American Mineralogist, Volume 103, pages 848–856, 2018

Relationships between unit-cell parameters and composition for rock-forming minerals on Earth, Mars, and other extraterrestrial bodies

Shaunna M. Morrison[1,2,*,†], Robert T. Downs[1], David F. Blake[3], Anirudh Prabhu[4], Ahmed Eleish[4], David T. Vaniman[5], Douglas W. Ming[6], Elizabeth B. Rampe[6], Robert M. Hazen[2], Cherie N. Achilles[1], Allan H. Treiman[7], Albert S. Yen[8], Richard V. Morris[6], Thomas F. Bristow[3], Steve J. Chipera[9], Philippe C. Sarrazin[10], Kim V. Fendrich[11], John Michael Morookian[8], Jack D. Farmer[12], David J. Des Marais[3], and Patricia I. Craig[7]

[1]University of Arizona, 1040 E 4th Street, Tucson, Arizona 85721, U.S.A.
[2]Geophysical Laboratory, Carnegie Institution, 5251 Broad Branch Road NW, Washington, D.C. 20015, U.S.A.
[3]NASA Ames Research Center, Moffett Field, California 94035, U.S.A.
[4]Rensselaer Polytechnic Institute (RPI) 110 Eighth Street, Troy, New York 12180, U.S.A.
[5]Planetary Science Institute, 1700 E. Fort Lowell, Tucson, Arizona 85719-2395, U.S.A.
[6]NASA Johnson Space Center, Houston, Texas 77058, U.S.A.
[7]Lunar and Planetary Institute, 3600 Bay Area Boulevard, Houston, Texas 77058, U.S.A.
[8]Jet Propulsion Laboratory, California Institute of Technology, 4800 Oak Grove Drive, Pasadena, California 91109, U.S.A
[9]Chesapeake Energy Corporation, 6100 N. Western Avenue, Oklahoma City, Oklahoma 73118, U.S.A.
[10]SETI Institute, Mountain View, California 94043, U.S.A.
[11]American Museum of Natural History, New York, New York 10024, U.S.A.
[12]Arizona State University, Tempe, Arizona 85281, U.S.A.

Abstract

Mathematical relationships between unit-cell parameters and chemical composition were developed for selected mineral phases observed with the CheMin X-ray diffractometer onboard the Curiosity rover in Gale crater. This study presents algorithms for estimating the chemical composition of phases based solely on X-ray diffraction data. The mineral systems include plagioclase, alkali feldspar, Mg-Fe-Ca $C2/c$ clinopyroxene, Mg-Fe-Ca $P2_1/c$ clinopyroxene, Mg-Fe-Ca orthopyroxene, Mg-Fe olivine, magnetite, and other selected spinel oxides, and alunite-jarosite. These methods assume compositions of Na-Ca for plagioclase, K-Na for alkali feldspar, Mg-Fe-Ca for pyroxene, and Mg-Fe for olivine; however, some other minor elements may occur and their impact on measured unit-cell parameters is discussed. These crystal-chemical algorithms can be applied to material of any origin, whether that origin is Earth, Mars, an extraterrestrial body, or a laboratory.

Keywords: X-ray diffraction, crystal chemistry, unit-cell parameters, plagioclase, olivine, pyroxene, magnetite, spinel, jarosite, alunite, Mars, Gale crater, Mars Science Laboratory, CheMin; Martian Rocks and Minerals: Perspectives from Rovers, Orbiters, and Meteorites

Introduction

The Chemistry and Mineralogy (CheMin) X-ray diffraction (XRD) instrument onboard the Mars Science Laboratory (MSL) rover, Curiosity, is employed by the MSL Science Team to analyze martian rock and sediment samples in Gale crater, Mars (Bish et al. 2013, 2014; Blake et al. 2013; Treiman et al. 2014, 2016; Vaniman et al. 2014; Bristow et al. 2015; Morris et al. 2016; Rampe et al. 2017; Yen et al. 2017; Achilles et al. 2017). XRD data obtained from CheMin allow mineral phase identification and refinement of unit-cell parameters and relative phase abundances. Information regarding phase chemical composition is useful in characterizing the geologic history of a rock unit, region, or planet. We studied the relationships between unit-cell parameters and chemical composition to constrain the composition of mineral phases observed in Gale crater. While these crystal-chemical algorithms were created with the purpose of studying Mars, they can be applied to any similar crystalline material regardless of origin.

To develop these crystal-chemical algorithms, we exploited the systematic relationship between atomic radii and unit-cell dimensions. Unit-cell lengths vary with chemical composition due to corresponding changes in atomic radii; therefore, measured unit-cell parameters provide insight into mineral composition and, in many cases, can be used to provide accurate estimates of anion composition. These systematics have been the focus of many mineralogical and XRD studies of synthetic and natural rock-forming minerals (Yoder and Sahama 1957; Bambauer et al. 1967; Louisnathan and Smith 1968; Matsui and Syono 1968; Fisher and Medaris 1969; Jahanbagloo 1969; Nolan 1969; Rutstein and Yund 1969; Turnock et al. 1973; Smith 1974; Schwab and Kustner 1977; Kroll 1983; Kroll and Ribbe 1983; Angel et al. 1990, 1998). Some research, such as the work on olivine by Yoder and Sahama (1957) and

* E-mail: shaunnamm@email.arizona.edu
† Special collection papers can be found online at http://www.minsocam.org/MSA/AmMin/special-collections.html.
Open access: Article available to all readers online.

0003-004X/18/0006–848$05.00/DOI: http://dx.doi.org/10.2138/am-2018-6123

Fisher and Medaris (1969), focused on the position of the single most prominent diffraction peak for determining the chemical composition of unidentified phases. The principal reasons for using a single-peak technique are the relative ease of measurement and the difficulty in calculating unit-cell parameters from diffraction data prior to the widespread use of computers and the adoption of full-pattern fitting methods such as Rietveld refinement. Some subsequent studies, such as the work on pyroxenes by Turnock et al. (1973) and Angel et al. (1998), used high-resolution diffraction patterns to estimate chemical composition based entirely on refined cell parameters.

In this study, we present algorithms to estimate the chemical composition of minerals based solely on unit-cell parameters. We developed algorithms for plagioclase, alkali feldspar, Mg-Fe-Ca pyroxene, Fe-Mg olivine, magnetite and related spinel oxides, and alunite-jarosite group phases by least-squares regression of known unit-cell parameters and composition. Additionally, we employed minimization routines for the crystal-chemical relationships of Mg-Fe-Ca pyroxenes. These studies were conducted with mineralogical data from many literature sources, with special attention to previous crystal-chemical studies, and also from the RRUFF Project (Lafuente et al. 2015). These data are publicly available at https://rruff.info/ima, and are compiled in Appendix[1] 1 and at https://github.com/shaunnamm/regression-and-minimization. The chemical variation and abundance of phases in this mineralogical database provide a comprehensive list of unit-cell parameters and associated composition, which can be harvested to produce robust chemical relationships. Their application to refined CheMin unit-cell parameters of martian minerals is reported in Morrison et al. (2018).

Crystal chemistry

This study incorporates unit-cell parameters and composition of minerals reported in previous studies as well as those documented in the RRUFF Project database (Lafuente et al. 2015) (Appendix[1] 1). The availability of large databases, such as RRUFF, to evaluate compositional systematics has increased the accuracy of estimated phase composition relative to previous studies. The following sections detail these crystal-chemical systematics and the resulting equations offer robust algorithms for estimating mineral composition from X-ray diffraction data. All calculations were performed in R; the R code is provided at https://github.com/shaunnamm/regression-and-minimization. The models selected in the sections below minimize the residual standard error, σ_{SE}, and contain only significant parameters (p-value >0.05). Where applicable, the residual standard error is given; the full error analysis procedure is detailed in Appendix[1] 2. To limit bias in the models generated by least-squares regression, we averaged the unit-cell parameters of samples with identical compositions. However, the full (not averaged) data sets were used in error determinations. Where applicable, cross-validation was used to assess whether these algorithms can be generalized to other data sets, and to recognize any over-fitting. Cross-validation was performed by training the model on 80% of the data and testing on the remaining 20% with 1000 iterations. Errors reported from cross-validation represent the average of the 1000 iterations. The coefficients in the equations listed throughout result in precision to the fourth decimal place for composition (apfu), the fifth decimal place for *a*, *b*, and *c* (Å), and the third decimal place for β (°); more digits can be obtained by specifying the number of desired digits in the R code.

Feldspar

Feldspar, variety plagioclase, is the most abundant mineral detected in 12 of the 13 Gale crater samples analyzed by CheMin as of June 2016. Alkali feldspar, variety sanidine, is found in significantly lower quantities than plagioclase in all but one of the 13 CheMin samples. Substitutions of minor elements is relatively common in potassium feldspar and less so in the plagioclase system. In alkali feldspar, minor amounts of other components can be present in a sample without causing the *b* and *c* unit-cell parameters to deviate noticeably from the Na-K trend. For example, alkali feldspars with cell dimensions that correspond to pure Na-K feldspar have been shown to contain Ba and Cs up to 0.02 atoms per formula unit (apfu) (Angel et al. 2013) and Rb up to 0.008 apfu (Dal Negro et al. 1978). In lunar K-feldspar, as much as 0.18 Ba apfu has been detected (Papike et al. 1998). However, Ba in martian meteorites has not been detected above 0.05 apfu and only 0.006% of the ~1000 martian meteorite feldspars contained any measurable Ba (Papike et al. 2009; Santos et al. 2015; Wittmann et al. 2015; Nyquist et al. 2016; Hewins et al. 2017). Additionally, sanidine can incorporate significant Fe^{3+} in the tetrahedral site, up to 0.698 Fe^{3+} apfu (Kuehner and Joswiak 1996; Linthout and Lustenhouwer 1993; Lebedeva et al. 2003). However, when the abundance of Fe^{3+} exceeds 0.1 apfu, the *b* unit-cell parameter increases beyond 13.05 Å and noticeably deviates from the trends shown in the alkali feldspar section below (Best et al. 1968; Lebedeva et al. 2003). Hewins et al. (2017) reported as much as 0.09 Fe^{3+} apfu in martian meteorite feldspar, an abundance that is unlikely to be detectable by examination of unit-cell parameters. In the plagioclase system, Fe^{2+} has been reported in abundance of 0.01–0.02 apfu from localities in Mexico and Japan (https://rruff.info), with no noticeable deviation from Na-Ca plagioclase unit-cell parameter trends. Matsui and Kimata (1997) synthesized anorthite with 0.196 Mn apfu; the resulting unit-cell parameters are significantly smaller than those of Na-Ca plagioclase and therefore such a composition can be easily distinguished from a pure Na-Ca phase. Of the martian meteorite feldspars with plagioclase composition (Papike et al. 2009; Santos et al. 2015; Wittmann et al. 2015; Nyquist et al. 2016; Hewins et al. 2017), 97.6% contain less than 2 wt% minor oxides (e.g., Fe_2O_3, K_2O, MgO, MnO, TiO_2, BaO).

Plagioclase

Previous plagioclase crystal-chemical studies reported trends in solid solution composition ($NaAlSi_3O_8$-$CaAl_2Si_2O_8$) with unit-cell parameters (Bambauer et al. 1967; Smith 1974; Kroll 1983), and examined the relationship between composition and tetrahedral bond lengths to investigate ordering systematics (Angel et al. 1990). Here, we correlate unit-cell parameters and composition of Na-Ca plagioclase. We performed statistical analyses on 49 relatively pure (≤0.042 K apfu) plagioclase samples (Supplemental[1] Table A1a), excluding the high-Ca plagioclase phases in which ordering results in a doubled *c* cell edge. We determined that Na-Ca plagioclase chemical composition can be estimated by a multivariate least-squares regression of the quadratic relationship between Ca- or Na-content and *a*, *b*, *c*, and β (Supplemental[1] Figs.

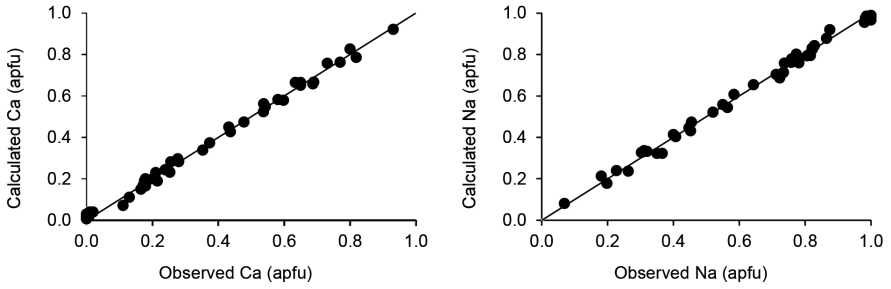

◀**FIGURE 1.** (**a**–**b**) Plagioclase Ca- and Na-content: calculated vs. observed. RMSE: Ca = 0.022 apfu; Na = 0.023 apfu.

A3a–3d) with a residual standard error of 0.022 and 0.023 apfu for Ca and Na, respectively (Eqs. 1a–1b). Note that only one of the equations below (1a and 1b) is needed to calculate the Ca-Na composition of plagioclase, the other component can be calculated by difference).

$$\text{Ca (apfu)} = -2480.385933a + 152.3540556a^2 + 1505.941326b - 58.71571613b^2 - 11.40375c - 0.003078067\beta^2 - 10.4185945\gamma + 0.057444444\gamma^2 + 1034.7951 \quad (1a)$$

$$\text{Na (apfu)} = 2025.35688a - 124.5278585a^2 - 1255.2328597b + 48.96341472b^2 + 9.244327c + 0.0033346038\beta^2 + 8.63542135\gamma - 0.04765164\gamma^2 - 691.81443. \quad (1b)$$

Equations 1c and 1d result in correlated estimates of Al- and Si-content, respectively:

$$\text{Al (afpu)} = 1 + \text{Ca (apfu)} \quad (1c)$$

$$\text{Si (apfu)} = 3 - \text{Ca (apfu)}. \quad (1d)$$

The accuracy of Equations 1a and 1b is demonstrated by comparing the observed Ca- and Na-content vs. calculated Ca- and Na-content (Figs. 1a–1b) and calculating the root-mean-square error (RMSE = 0.022 Ca apfu and 0.024 Na apfu; cross-validation RMSE = 0.024 Ca apfu and 0.027 Na apfu). Plagioclase regression data are shown in Supplemental[1] Table A1a.

ALKALI FELDSPAR

Previous alkali feldspar studies extensively examined and characterized the relationship between composition, site ordering, and unit-cell parameters (Kroll and Ribbe 1983). Kroll and Ribbe (1983) primarily focused on the effects of composition and Al/Si ordering in the tetrahedral sites. In this study, we followed the same principles and similar techniques, while focusing strictly on unit-cell parameters and their direct relationship to composition and fractional order-disorder. To characterize fully the composition and ordering of Ca-free alkali feldspars, we constructed a quadrilateral (Fig. 2) similar to that of Kroll and Ribbe (1983). We used well-characterized alkali feldspar end-members (Kroll and Ribbe 1983), low microcline, high sanidine, low albite, and high albite (Supplemental[1] Table A1b), to assemble the quadrilateral diagram; these end-members were also used to derive the algorithm (Eqs. 2a–2b) for computing composition and ordering (1 = fully ordered; 0 = fully disordered). Note that this model assumes a composition along the Na-K solid solution and does not account for any potential celsian ($BaAl_2Si_2O_8$) component.

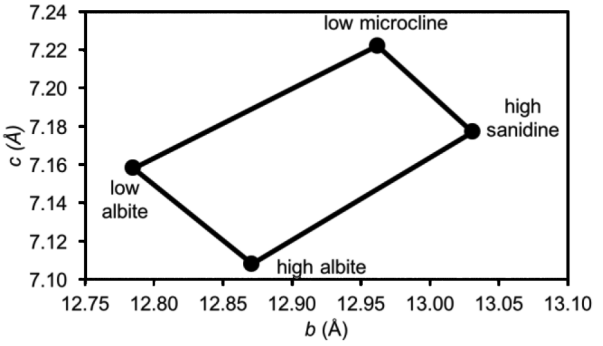

FIGURE 2. Alkali feldspar quadrilateral: composition and Al-Si ordering as a function of *c* and *b* unit-cell parameters. Black circles represent literature end-members. Composition trends from $NaAlSi_3O_8$ at the low albite–high albite edge to $KAlSi_3O_8$ at the low microcline–high sanidine edge. Al-Si ordering trends from completely ordered at the low albite–low microcline edge to completely disordered at the high albite–high sanidine edge.

$$\begin{bmatrix} -3.76223 & -5.76875 & 90.42789 \\ -5.76875 & 13.37681 & -20.8328 \\ 0 & 0 & 1 \end{bmatrix} \begin{bmatrix} b \\ c \\ 1 \end{bmatrix} = \begin{bmatrix} \text{Na (apfu)} \\ \text{ordering} \\ 1 \end{bmatrix} \quad (2a)$$

$$\text{K (apfu)} = 1 - \text{Na (apfu)}. \quad (2b)$$

PYROXENE

To date, three distinct pyroxene phases have been detected in Gale crater by CheMin: (1) augite, ideally $(Ca,Mg,Fe)_2Si_2O_6$, with *C*2/*c* symmetry; (2) pigeonite, ideally $(Mg,Fe,Ca)_2Si_2O_6$, with $P2_1/c$ symmetry; and (3) orthopyroxene, ideally $(Mg,Fe)_2Si_2O_6$, with *Pbca* symmetry (Bish et al. 2013, 2014; Blake et al. 2013; Treiman et al. 2014, 2016; Vaniman et al. 2014; Morris et al. 2016; Rampe et al. 2017; Yen et al. 2017; Achilles et al. 2017).

In previous studies of pyroxenes, two approaches were used to correlate X-ray diffraction data with chemical composition. The first approach focused on correlations between lattice spacings and composition (Rutstein and Yund 1969). The second approach used the relationships between unit-cell parameters and composition (Nolan 1969; Rutstein and Yund 1969; Turnock et al. 1973; Angel et al. 1998). Here, we use the latter approach in conjunction with minimization to characterize systematic relationships between unit-cell parameters and Mg-Fe-Ca composition (Supplemental[1] Figs. A3e–A3ab). When applied to our data set, our algorithms yield decreased uncertainty relative to previous studies (Table 1).

TABLE 1. Root-mean-square error (RMSE) of estimated Mg-content in pyroxene subsets, based on data from Supplemental[1] Tables A1c–A1e

	Mg (apfu)	Fe (apfu)	Ca (apfu)
	C*2/*c		
This study	0.037	0.049	0.030
Turnock et al. (1973)	0.045	0.079	0.056
Rutstein and Yund (1969) all/Ca = 1[a]	0.221/0.032	0.202/0.032	0.291/NA
	P*2$_1$/*c		
This study	0.041	0.045	0.026
Turnock et al. (1973)	0.070	0.067	0.045
Angel et al. (1998) all/Ca-free[b]	0.076/0.036	0.277/0.036	0.235/NA
	Pbca		
This study	0.053	0.049	0.021
Turnock et al. (1973)	0.088	0.115	0.043

Note: This study's methods compared with selected previous studies.
[a] The algorithm presented in Rutstein and Yund (1969) is specifically for *C*2/*c* pyroxenes with Ca = 1 apfu. Therefore, we applied it both to our whole data set (Supplemental[1] Tables A1c–A1e) and to a subset with Ca = 1 apfu.
[b] The algorithm presented in Angel et al. (1998) is specifically for Ca-free *P*2$_1$/*c* pyroxenes. Therefore, we applied it both to our whole data set (Supplemental[1] Tables A1c–A1e) and to a Ca-free subset.

Martian high-Ca pyroxenes (Ca mole fraction >0.2, based on Ca, Fe, Mg, and Mn) generally have relatively low abundances of non-quadrilateral components (e.g., Papike et al. 2009) compared to terrestrial high-Ca pyroxenes (e.g., Robinson 1980; Papike 1980). Given that the main focus of the current work is on inferring pyroxene chemistry from XRD data acquired by the Curiosity rover in Gale crater, Mars, we limit our discussion of non-quadrilateral components to martian pyroxenes. Of the 876 high-Ca pyroxene analyses from martian meteorites reported in Papike et al. (2009), Santos et al. (2015), Wittmann et al. (2015), Nyquist et al. (2016), and Hewins et al. (2017), only 0.2% contain more than 10% non-quadrilateral components (as defined in Cameron and Papike 1981). None of the 1680 low-Ca pyroxene analyses of martian meteorites (Papike et al. 2009; Santos et al. 2015; Wittmann et al. 2015; Nyquist et al. 2016; Hewins et al. 2017) contain more than 10% non-quadrilateral components and only 1.4% contain more than 5% non-quadrilateral cations. Due to the fact that non-quadrilateral components can have ionic radii (and, consequently, unit-cell parameters) both greater than and less than Mg, Fe, and Ca (Baker and Beckett 1999), it is difficult to determine a unique chemistry based strictly on unit-cell parameters. Therefore, we limit our algorithms below to the Mg-Fe-Ca pyroxene system, with the understanding that there may be small amounts of non-quadrilateral cations that remain undetected by this method. To help the reader determine if their samples lie significantly outside of the Mg-Fe-Ca system, we have determined the maximum χ^2 value (χ^2_{max}) for the *a*, *b*, and β unit-cell parameters in each pyroxene data set based on Equations 4a, 4b, 4d, 5a, 5b, 5d, 6a, and 6b below (χ^2_{max}: *C*2/*c* = 0.00026; *P*2$_1$/*c* = 0.00043; *Pbca* = 0.000028) and recommend exercising caution when the χ^2 value of a data set exceeds ~3 × χ^2_{max} because there is a possibility of non-quadrilateral components.

This study incorporated three data sets containing a total 140 pyroxene compositions and corresponding unit-cell parameters (86 *C*2/*c*, 52 *P*2$_1$/*c*, and 41 *Pbca*) (Supplemental[1] Tables A1c–A1e). Although the compositions of Fe-Mg-Ca pyroxenes are roughly a linear function of select unit-cell parameters, the relationships between composition and cell parameters are more accurately characterized by accounting for non-linearity. To determine the best relationship between the unit-cell parameters and composition, we began with the functional form presented in Turnock et al. (1973):

$$\text{Clinopyroxene: } z = c_0 + c_1Mg + c_2Ca + c_3Mg^2 + c_4MgCa + c_5Ca^2 + c_6Mg^3 + c_7Mg^2Ca + c_8MgCa^2 + c_9Ca^3 \quad (3a)$$

$$\text{Orthopyroxene: } z = c_0 + c_1Mg + c_2Ca + c_3Mg^2 + c_4Ca^2 + ... + c_nMg^n + c_{n+1}Ca^n. \quad (3b)$$

where z is the unit-cell parameter (either *a*, *b*, *c*, or β), c_i (i = 0 to 9) are the coefficients, and n is 3, 2, and 2 for *a*, *b*, and *c*, respectively. Note that Mg and Ca apfu are used in place of the molar compositional parameters, Fe/(Fe+Mg) and Ca/(Ca+Fe+Mg), that were used by Turnock et al. (1973); additionally, Equation 3b is expanded to include Ca, whereas Turnock et al. (1973) used Ca-free orthopyroxene.

We then tested the accuracy of reproducing the measured unit-cell parameters with Equations 3a and 3b and every permutation of variables to determine the most accurate functions of z. The resulting functions are given are given below in Equations 4a–4d, 5a–5d, and 6a–6c.

Employing Equations 4a–4d, 5a–5d, and 6a–6c, we performed a minimization of the weighted sum of squared error ($\Sigma\sigma^2$) to estimate pyroxene chemical composition. We used a bounded [0 ≤ Mg (apfu) ≤ 2; 0 ≤ Ca (apfu) ≤ 2] PORT optimization (Gay 1990) with starting parameters of Mg = 2 and Ca = 1. Fe calculated post-minimization and is equal to two minus the sum of Mg and Ca. We began by using all available unit-cell parameters in the minimization routine (Eq. 7a for the clinopyroxenes and 7b for orthopyroxenes).

$$\Sigma\sigma^2 = [(a - a_{calc})/(a_{calc}/\beta_{calc})]^2 + (b - b_{calc})/(b_{calc}/\beta_{calc})^2 + (c - c_{calc})/(c_{calc}/\beta_{calc})^2 + (\beta - \beta_{calculated})^2 \quad (7a)$$

$$\Sigma\sigma^2 = [(a - a_{calc})/(a_{calc}/b_{calc})]^2 + (b - b_{calc})^2 + (c - c_{calc})/(c_{calc}/b_{calc})^2. \quad (7b)$$

We tested every permutation of unit-cell parameter combinations for the minimization (Eqs. 7a–7b) and found that the lowest error resulted from a combination of *a*, *b*, and β for clinopyroxenes (Eq. 8a) and *a* and *b* for orthopyroxene (Eq. 8b).

$$\Sigma\sigma^2 = [(a - a_{calc})/(a_{calc}/\beta_{calc})]^2 + (b - b_{calc})/(b_{calc}/\beta_{calc})^2 + (\beta - \beta_{calculated})^2 \quad (8a)$$

$$\Sigma\sigma^2 = [(a - a_{calc})/(a_{calc}/b_{calc})]^2 + (b - b_{calc})^2. \quad (8b)$$

The accuracy of the minimization method is demonstrated by plotting the observed Mg-, Ca-, and Fe-contents vs. their calculated values (Figs. 3a–3c, 4a–4c, and 5a–5c). Errors associated with the above method are in Table 1.

Note that Turnock et al. (1973) did not distinguish between *P*2$_1$/*c* and *C*2/*c* pyroxenes in their algorithms; we tested this approach by combining all clinopyroxenes and performing the above regressions and minimization. However, the associated error (RMSE: Mg = 0.067 apfu, Ca = 0.090 apfu, Fe = 0.110 apfu) was significantly greater than when *P*2$_1$/*c* and *C*2/*c* pyroxenes are treated separately. This difference is likely due to changes in the β trend between space groups (Turnock et al. 1973).

Augite; *C*2/*c*:

a (Å) = –0.106429Mg + 0.074932Ca + 0.016032Mg^2 + 0.1206MgCa + 0.03144Ca^3– 0.129102MgCa^2 + 9.74681 (4a)
b (Å) = –0.25789Mg – 0.212528Ca + 0.040693Mg^2 + 0.08659Ca^2 + 0.16962MgCa –0.055575MgCa^2 + 9.16081 (4b)
c (Å) = –0.142494Ca – 0.0421695Mg^2 + 0.107222Ca^2 + 0.109804MgCa + 0.040853Mg^{2}Ca – 0.107327MgCa^2 + 5.28441 (4c)
β (°) = 4.405Mg – 3.426Mg^2 – 7.546Ca^2 – 4.2137MgCa + 0.6875Mg^3 + 4.736Ca^3 +2.2772Mg^{2}Ca + 1.3864MgCa^2 + 107.599 (4d)

Residual standard error: Equation 4a = 0.006 Å, 4b = 0.005 Å, 4c = 0.004 Å, 4d = 0.11 Å. RMSE: Equation 4a = 0.005 Å (cross-validation: 0.008 Å), 4b = 0.003 Å (cross-validation: 0.006 Å), 4c = 0.006 Å (cross-validation: 0.009 Å), 4d = 0.05° (cross-validation: 0.19°).

Pigeonite; $P2_1/c$:

a (Å) = –0.050902Mg + 0.21487Ca – 0.1471Ca^2 – 0.05754MgCa + 0.04501Mg^{2}Ca + 9.7121 (5a)
b (Å) = –0.1751943Mg + 0.0201938Mg^2 – 0.03603Ca^2 + 0.0284Mg^{2}Ca + 9.086603 (5b)
c (Å) = 0.0910769Ca – 0.0296873Mg^2 – 0.17699Ca^2 + 0.145384MgCa + 0.007397Mg^3 – 0.04537Mg^{2}Ca + 5.23027 (5c)
β (°) = 0.6804Mg – 4.2167Ca – 0.64465Mg^2 + 7.2514MgCa + 0.14102Mg^3 – 2.3217Mg^{2}Ca – 4.187MgCa^2 + 108.4444 (5d)

Residual standard error: Equations 5a = 0.007 Å, 5b = 0.006 Å, 5c = 0.008 Å, 5d = 0.09°. RMSE: Equations 5a = 0.006 Å (cross-validation: 0.008 Å), 5b = 0.002 Å (cross-validation: 0.006 Å), 5c = 0.010 Å (cross-validation: 0.014 Å), 5d = 0.04° (cross-validation: 0.10°).

Orthopyroxene; *Pbca*:

a (Å) = –0.14978Mg + 0.7807Ca + 0.025194Mg^2 – 4.863Ca^2 + 18.42965 (6a)
b (Å) = –0.17051Mg + 0.01951Mg^2 + 9.08082 (6b)
c (Å) = –0.01007Mg + 0.31524Ca – 0.00982Mg^2 – 2.89809Ca^2 + 5.23733 (6c)

Residual standard error: Equations 6a = 0.013 Å, 6b = 0.008 Å, 6c = 0.005 Å. RMSE: Equations 6a = 0.012 Å (cross-validation: 0.015 Å), 6b = 0.007 Å (cross-validation: 0.008 Å), 6c = 0.004 Å (cross-validation: 0.006 Å).

OLIVINE

As of June 2016, CheMin has detected an olivine phase in three of the thirteen Gale crater samples. Numerous studies have examined the systematics of olivine composition in relation to X-ray diffraction data (Table 2). Some of these studies focused on the correlation between composition and the position of the most intense single diffraction peak, d_{130} (Yoder and Sahama 1957; Fisher and Medaris 1969; Schwab and Kustner 1977). Other studies examined the relationship between composition and unit-cell parameters (Louisnathan and Smith 1968; Matsui and Syono 1968; Jahanbagloo 1969). Following the success of the latter method, our study focused on the crystal-chemical systematics of Fe-Mg olivine unit-cell parameters vs. composition.

We incorporated unit-cell parameters and measured compositional data from 60 olivine samples, including those reported by previous olivine crystal-chemistry studies (Supplemental[1] Table A1f). Our data were limited to those samples containing only Mg and Fe. Distinguishing Fe-Mg-only olivine from those containing Ca or Mn (Supplemental[1] Table A1g) is difficult, and sometimes not possible, with unit-cell parameters alone. If Ca exceeds 0.5 apfu, the b parameter increases dramatically (>10.80 Å), confirming that the sample is not in the Fe-Mg or Fe-Mg-Mn system. Likewise, as evident in Figure 6, if b or V exceed 10.50 Å or 308 Å^3, respectively, the sample is outside of the Mg-Fe-only system. However, samples within the Mg-Fe-only unit-cell parameter range (b = 10.19–10.50 Å; V = 289–308 Å^3) can contain up to 0.19 Ca apfu and 1 Mn apfu, according to literature data in Supplemental[1] Table A1g. In evaluating Gale crater olivine, we can limit our compositional range to that reported in martian meteorites: Mn < 0.038 apfu and Ca < 0.027 apfu (Papike et al. 2009; Hewins et al. 2017).

TABLE 2. Root-mean-square error (RMSE) of estimated Mg-content in olivine, based on data from Supplemental[1] Table A1f

Study	RMSE (Mg apfu)
Equation 9a, this study	0.017
Yoder and Sahama (1957)	0.064
Louisnathan and Smith (1968)	0.036
Fisher and Medaris (1969)	0.029
Jahanbagloo (1969)	0.062
Schwab and Kustner (1977)	0.024

Note: Equation 9a compared with selected previous studies.

A linear least-squares regression of Mg- and Fe-content vs. b in olivine (Supplemental[1] Figs. A4ac–A4af) resulted in the expressions 6a and 6b for estimating the chemical composition of Mg-Fe olivine. Note that only one of the equations below (9a and 9b) is needed to calculate the Fe-Mg composition of olivine, the other component can be calculated by difference. The residual standard error of Mg and Fe is 0.018 and 0.018 apfu, respectively.

Mg (apfu) = –7.15567b + 74.9756 (9a)
Fe (apfu) = 7.156854b – 72.98787. (9b)

The RMSE of the observed vs. calculated Mg- and Fe-content in olivine samples used in this study (Figs. 7a–7b) is 0.017 and 0.017 apfu (0.018 and 0.018 apfu in cross-validation), respectively.

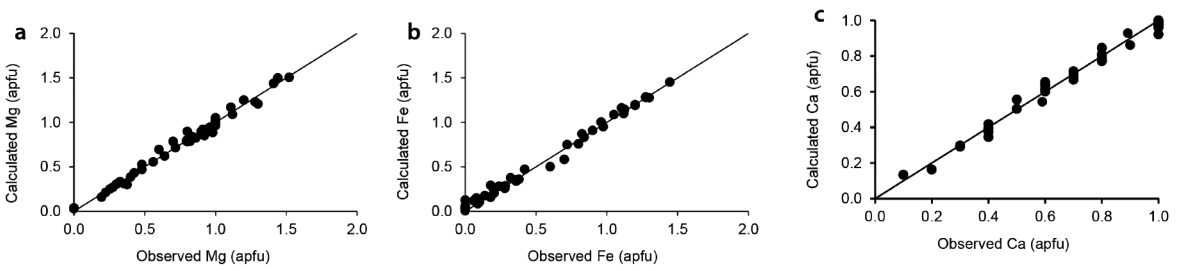

FIGURE 3. (**a**–**c**) Augite Mg-, Fe-, and Ca-content: calculated vs. observed. Mg, Fe, and Ca RMSE = 0.037, 0.049, and 0.030 apfu, respectively.

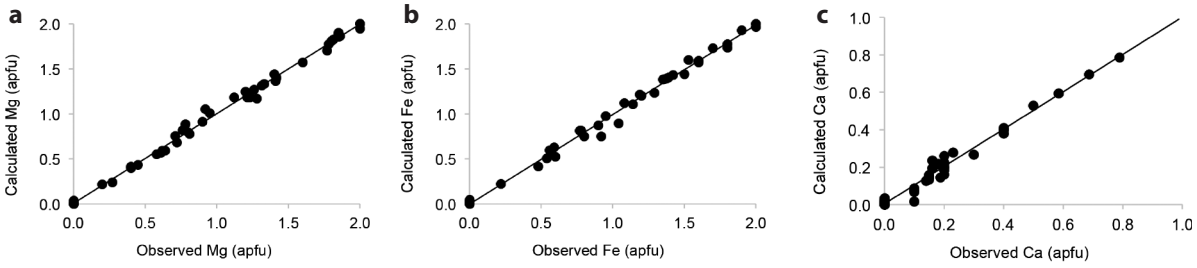

FIGURE 4. (**a**–**c**) Pigeonite Mg-, Fe-, and Ca-content: calculated vs. observed. Mg, Fe, and Ca RMSE = 0.041, 0.045, and 0.026 apfu, respectively.

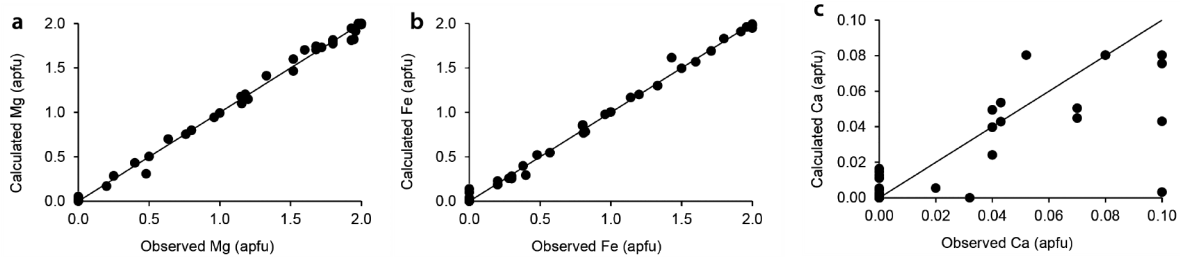

FIGURE 5. (**a**–**c**) Orthopyroxene Mg-, Fe-, and Ca-content: calculated vs. observed. Mg, Fe, and Ca RMSE = 0.053, 0.049, and 0.021 apfu, respectively.

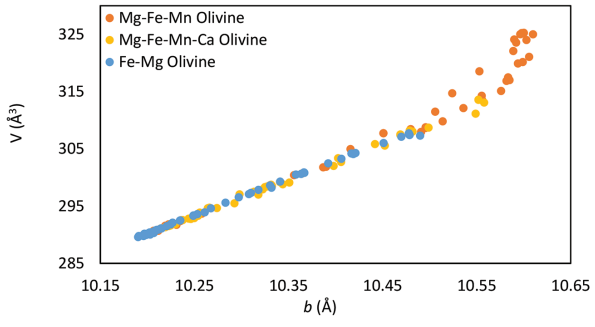

FIGURE 6. Mg-Fe, Mg-Fe-Mn, and Mg-Fe-Mn-Ca (with Ca < 0.5 apfu) olivine *b* unit-cell parameter vs. unit-cell volume, *V*.

MAGNETITE AND SELECTED SPINEL OXIDES

As of June 2016, each Gale crater samples analyzed by CheMin contains a spinel phase. In nature, the cubic spinel oxide structure can accommodate various elements, including transition elements Fe, Ti, Cr, Mn, Co, Cu, Zn, V, and Ni, as well as metals, metalloids, and non-metals such as Mg, Ca, Si, Al, Ge, Sb, and it can also exhibit site vacancy (□). Chromite

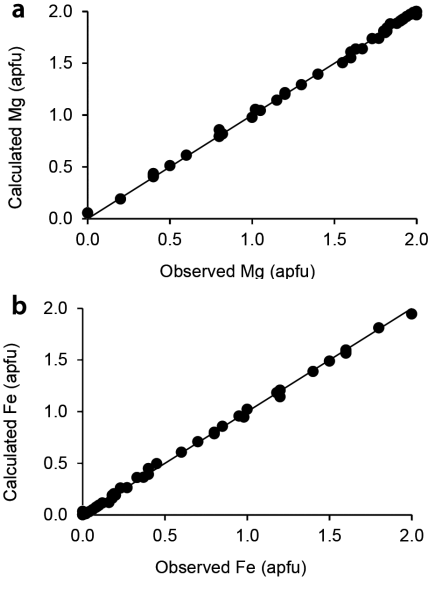

FIGURE 7. (**a**–**b**) Olivine Mg- and Fe-content: calculated vs. observed. RMSE = 0.017 Mg apfu and 0.017 Fe apfu.

accounts for ~18% of the spinel phases observed in the martian meteorites studied in the 64 references cited in Appendix[1] 4. There are also significant amounts of Al-rich (up to 27.85 wt% Al_2O_3 or 1.01 Al apfu, assuming no site vacancy), Ti-rich (up to 33.8 wt% TiO_2/0.95 Ti apfu), and Mg-rich (up to 9.03 wt% MgO/0.43 Mg apfu) magnetite. Only ~2% have more than 0.50 Al apfu, but ~21% have more than 0.50 Ti apfu, and ~35% have more than 1.00 Cr apfu. Si, V, Mn, Ca, Na, Ni, Co, and Zn have been detected, but in relatively small amounts (<0.05 apfu). In addition to martian meteorite data, the MER Mössbauer spectrometers have also collected information on spinel phases at Gusev crater and Meridiani Planum and found them to be of magnetite ($Fe^{2+}Fe^{3+}_2O_4$) or Ti-magnetite composition, with some minor chromite ($Fe^{2+}Cr_2O_4$) (Morris et al. 2006a, 2006b, 2008). Therefore, when evaluating Gale crater samples, we can have some confidence that the spinel phase is likely in the Fe, Fe-Ti, or Fe-Cr systems, or a mixture thereof.

While some of spinel compositional space is not relevant to martian samples, it may be to samples of other origins; therefore, we considered it important to characterize the common spinel systems. To characterize the crystal-chemical relationships in spinel phases, we compiled crystallographic and compositional data (Supplemental[1] Table A1h) and observed that Al, Ti, Mg, Mn, Cr, Ni, Zn, and V were frequently reported as major components of magnetite. In addition to magnetite (Fe_3O_4), other end-member spinel oxides include maghemite ($Fe_{2.67}O_4$), hercynite ($Fe^{2+}Al_2O_4$), ulvöspinel ($Fe^{2+}_2TiO_4$), magnesioferrite ($MgFe^{3+}_2O_4$), magnesiochromite ($MgCr^{3+}_2O_4$), chromite ($Fe^{2+}Cr_2O_4$), trevorite ($NiFe^{3+}_2O_4$), franklinite ($ZnFe^{3+}_2O_4$), and coulsonite ($Fe^{2+}V^{3+}_2O_4$). In Figure 8, the literature trends of Fe vs. the *a* unit-cell parameter are given for (Fe,□), (Fe,Al), (Fe,Ti), (Fe,Mg), (Fe,Cr), (Fe,Ni), (Fe,Zn), (Fe,V) (Fe,Al,□), (Fe,Mg,Al), (Fe,Mn,Ti), (Fe,Mg,Cr), and (Fe,Mg,Ti) phases. Data points with combinations other than those listed were excluded from Figure 8 for clarity and because the complexity of the trends increases significantly beyond 3 cations. The complexity of Figure 8, a result of variation in cation size and oxidation state of multi-element phases, illustrates that numerous chemical combinations can correlate with a given *a* cell edge in the spinel structure. Note that the (Mg,Fe) data are limited and there is not a linear trend; this complexity likely reflects cation ordering.

To interpret the possible composition of spinel oxide phases, we performed linear regressions of Fe-content vs. *a* for each of the trends shown in Figure 8 (Eqs. 10a–10m). Error metrics associated with each linear regression can be found in Table 3.

(Fe,□): $4.329809a - 33.4254 = \text{Fe (apfu)}$ (10a)
$3 - \text{Fe (apfu)} = \square\ \text{(pfu)}$

(Fe,Al): $8.230266a - 66.108983 = \text{Fe (apfu)}$ (10b)
$3 - \text{Fe (apfu)} = \text{Al (apfu)}$

(Fe,Ti): $-6.577146a + 58.16868 = \text{Fe (apfu)}$ (10c)
$3 - \text{Fe (apfu)} = \text{Ti (apfu)}$

(Fe,Mg): $74.172617a - 619.86623 = \text{Fe (apfu)}$ (10d)
$3 - \text{Fe (apfu)} = \text{Mg (apfu)}$

(Fe,Cr): $97.561a - 816.22 = \text{Fe (apfu)}$ (10e)
$3 - \text{Fe (apfu)} = \text{Cr (apfu)}$

(Fe,Ni): $17.802356a - 146.47258 = \text{Fe (apfu)}$ (10f)
$3 - \text{Fe (apfu)} = \text{Ni (apfu)}$

(Fe,Zn): $-22.6677979a + 193.3425374 = \text{Fe (apfu)}$ (10g)
$3 - \text{Fe (apfu)} = \text{Zn (apfu)}$

(Fe,V): $-35.714a + 302.89 = \text{Fe (apfu)}$ (10h)
$3 - \text{Fe (apfu)} = \text{Ni (apfu)}$

(Fe,Al,□): $\begin{bmatrix} 6.521577 & -51.8927 \\ -3.692257 & 31.05033 \end{bmatrix}\begin{bmatrix} a \\ 1 \end{bmatrix} = \begin{bmatrix} \text{Fe (apfu)} \\ \text{Al (apfu)} \end{bmatrix}$ (10i)
$3 - \text{Fe (apfu)} - \text{Al (apfu)} = \square\ \text{(pfu)}$

(Fe,Mg,Al): $\begin{bmatrix} 13.506902 & -109.20881 \\ -12.815325 & 104.6199886 \end{bmatrix}\begin{bmatrix} a \\ 1 \end{bmatrix} = \begin{bmatrix} \text{Fe (apfu)} \\ \text{Mg (apfu)} \end{bmatrix}$ (10j)
$3 - \text{Fe (apfu)} - \text{Mg (apfu)} = \text{Al (apfu)}$

(Fe,Mn,Ti): $\begin{bmatrix} -14.625663 & 126.9668 \\ 14.625663 & -124.9668 \end{bmatrix}\begin{bmatrix} a \\ 1 \end{bmatrix} = \begin{bmatrix} \text{Fe (apfu)} \\ \text{Mn (apfu)} \end{bmatrix}$ (10k)
$3 - \text{Fe (apfu)} - \text{Mn (apfu)} = \text{Ti (apfu)}$

(Fe,Mg,Cr): $\begin{bmatrix} 22.340604 & -186.14709 \\ -22.4088793 & 187.71818 \end{bmatrix}\begin{bmatrix} a \\ 1 \end{bmatrix} = \begin{bmatrix} \text{Fe (apfu)} \\ \text{Mg (apfu)} \end{bmatrix}$ (10l)
$3 - \text{Fe (apfu)} - \text{Mg (apfu)} = \text{Cr (apfu)}$

(Fe,Mg,Ti): $\begin{bmatrix} 26.893648 & -227.37053 \\ -25.412612 & 216.80734 \end{bmatrix}\begin{bmatrix} a \\ 1 \end{bmatrix} = \begin{bmatrix} \text{Fe (apfu)} \\ \text{Mg (apfu)} \end{bmatrix}$ (10m)
$3 - \text{Fe (apfu)} - \text{Mg (apfu)} = \text{Ti (apfu)}$

Above equations based on data sets with only two points do not have an associated value for σ_{SE} because there is no spread in the data. The uncertainty associated with these equations is based solely on the input unit-cell parameters (see Appendix[1] 2 for full error calculation).

Once the amount of Fe is estimated, the relative proportions of Fe^{2+} and Fe^{3+} can be computed by charge balance.

ALUNITE-JAROSITE

Alunite-jarosite group minerals are associated with secondary weathering and alteration of S-bearing deposits. The mineral phases are hexagonal with space group $R\bar{3}m$ and include alunite, $KAl_3(SO_4)_2(OH)_6$; jarosite, $KFe^{3+}_3(SO_4)_2(OH)_6$; natroal-

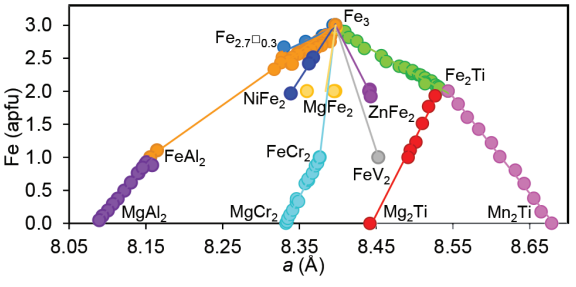

FIGURE 8. Selected spinel oxides (M_3O_4) as a function of Fe-content and *a* unit-cell parameter.

TABLE 3. Root-mean-square errors (RMSE), RMSE of cross-validation, and residual standard errors (σ_{SE}) associated with spinel linear models

Model	Anion	RMSE (apfu)	RMSE (apfu)[a]	σ_{SE} (apfu)
FeVacancy	Fe	0.038	0.081	0.047
FeAl	Fe	0.012	0.306	0.021
FeTi	Fe	0.029	0.031	0.030
FeMg	Fe	0.031	0.741	0.054
FeNi	Fe	0.016	0.041	0.022
FeZn	Fe	0.027	0.338	0.038
FeAlVacancy	Fe	0.040	0.042	0.042
FeAlVacancy	Al	0.058	0.060	0.059
FeMgAl	Fe	0.035	0.037	0.038
FeMgAl	Mg	0.026	0.027	0.028
FeMnTi	Fe	0.038	0.045	0.042
FeMnTi	Mn	0.038	0.045	0.042
FeMgCr	Fe	0.023	0.023	0.024
FeMgCr	Mg	0.023	0.024	0.025
FeMgTi	Fe	0.036	0.056	0.047
FeMgTi	Mg	0.030	0.046	0.039

[a] Cross-validation.

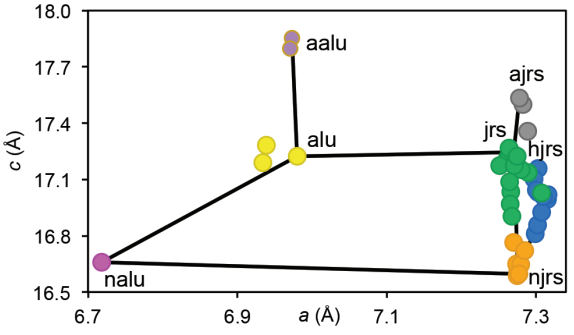

FIGURE 9. Alunite-jarosite phases as a function of *a* unit-cell parameter vs. *c* unit-cell parameter. jrs = jarosite, alu = alunite, njrs = natrojarosite, nalu = natroalunite, ajrs = ammoniojarosite, aalu = ammonioalunite, hjrs = hydronuiumjarosite.

unite, $NaAl_3(SO_4)_2(OH)_6$; natrojarosite, $NaFe^{3+}_3(SO_4)_2(OH)_6$; ammonioalunite, $NH_4Al_3(SO_4)_2(OH)_6$; ammoniojarosite, $NH_4Fe^{3+}_3(SO_4)_2(OH)_6$; and hydroniumjarosite, $(H_3O)Fe^{3+}_3(SO_4)_2(OH)_6$. Alunite-jarosite minerals have been discovered on Mars and offer clues about the weathering and alteration history of the martian surface (e.g., Klingelhöfer et al. 2004; Zolotov and Shock 2005; Morris et al. 2006a, 2006b; Golden et al. 2008; Swayze et al. 2008; Mills et al. 2013).

To identify which alunite-jarosite phases are present in samples analyzed by CheMin, we constructed an alunite-jarosite quadrilateral (Fig. 9) by examining the relationship between *a* and *c* unit-cell parameters (Supplemental[1] Table A1i). Due to the lack of orthogonality in the alunite-natroalunite-jarosite-natrojarosite quadrilateral, compositions falling on or within the quadrilateral are calculated with a series of equations (Eqs. 11a–11e).

$$\text{K (apfu)} = 1.654c - 27.508 \quad (11a)$$

$$\begin{bmatrix} -0.00923 & 7.46919 \\ 0.463717 & -0.966595 \end{bmatrix} \begin{bmatrix} c \\ 1 \end{bmatrix} = \begin{bmatrix} a_{jr} \\ a_{al} \end{bmatrix} \quad (11b)$$

$$\text{Fe}\left(\text{apfu}\right) = \frac{-3(a - a_{jr})}{a_{al} - a_{jr}} + 3 \quad (11c)$$

$$\text{Na (apfu)} = 1 - \text{K (apfu)} \quad (11d)$$

$$\text{Al (apfu)} = 3 - \text{Fe (apfu)} \quad (11e)$$

Alunite-jarosite group phase regression data are shown in Supplemental[1] Table A1i.

IMPLICATIONS

The methods provided in this study offer users the opportunity to estimate the chemical composition of select phases based solely on X-ray diffraction data. The mineral systems studied include the important rock-forming mineral groups of Na-Ca plagioclase, Na-K alkali feldspar, Mg-Fe-Ca clinopyroxene, Mg-Fe-Ca orthopyroxene, Mg-Fe olivine, magnetite and selected other spinel-group minerals, and alunite-jarosite phases. These algorithms are applicable to minerals of any origin, whether that origin be a laboratory, Earth, Mars, or any of the various solid objects in our solar system.

ACKNOWLEDGMENTS

We acknowledge the support of the JPL engineering and Mars Science Laboratory (MSL) operations team. The study benefited from discussions with Mike Baker concerning relationships between the compositions of olivine and pyroxene and their associated unit-cell parameters. We thank the reviewers of this manuscript, Olivier Gagné and Bradley Jolliff, for their insightful and constructive feedback. This research was supported by NASA NNX11AP82A, MSL Investigations, and by the National Science Foundation Graduate Research Fellowship under Grant No. DGE-1143953. Any opinions, findings, or recommendations expressed herein are those of the authors and do not necessarily reflect the views of the National Aeronautics and Space Administration or the National Science Foundation.

REFERENCES CITED

Achilles, C.N., Downs, R.T., Ming, D.W., Rampe, E.B., Morris, R.V., Treiman, A.H., Morrison, S.M., Yen, A.S., Vaniman, D.T., Blake, D.F., and others. (2017) Mineralogy of an Active Eolian Sediment from the Namib Dune, Gale crater, Mars. Journal of Geophysical Research: Planets, Bagnold Dunes Special Issue, 122, 2344–2361.

Angel, R.J., Carpenter, M.A., and Finger, L.W. (1990) Structural variation associated with compositional variation and order-disorder behavior in anorthite-rich feldspars. American Mineralogist, 75, 150–162.

Angel, R.J., McCammon, C., and Woodland, A.B. (1998) Structure, ordering and cation interactions in Ca-free $P2_1/c$ clinopyroxenes. Physics and Chemistry of Minerals, 25, 249–258.

Angel, R.J., Ross, N.L., Zhao, J., Sochalski-Kolbus, L., Krüger, H., and Schmidt, B.C. (2013) Structural controls on the anisotropy of tetrahedral frameworks: the example of monoclinic feldspars. European Journal of Mineralogy, 25(4), 597–614.

Baker, M.B., and Beckett, J.R. (1999) The origin of abyssal peridotites: a reinterpretation of constraints based on primary bulk compositions. Earth and Planetary Science Letters, 171(1), 49–61.

Bambauer, H.U., Corlett, M., Eberhard, E., and Viswanathan, K. (1967) Diagrams for the determination of plagioclases using X-ray powder methods (Part III of laboratory investigations of plagioclases). Schweizerische Mineralogische und Petrographische Mitteilungen, 47, 333–349.

Best, M.G., Henage, L.F., and Adams, J.A. (1968) Mica peridotite wyomingite and associated pottassic igneous rocks in Northeastern Utah. American Mineralogist, 53, 1041.

Bish, D.L., Blake, D.F., Vaniman, D.T., Chipera, S.J., Morris, R.V., Ming, D.W., Treiman, A.H., Sarrazin, P., Morrison, S.M., Downs, R.T., and others and MSL Science Team (2013) X-ray diffraction results from Mars Science Laboratory: Mineralogy of Rocknest at Gale Crater. Science, 27, 341, 1238932.

Bish, D., Blake, D., Vaniman, D., Sarrazin, P., Bristow, T., Achilles, C., Dera, P., Chipera, S., Crisp, J., Downs, R., and others. (2014) The first X-ray diffraction measurements on Mars. IUCrJ, 1, 514–522.

Blake, D.F., Morris, R.V., Kocurek, G., Morrison, S.M., Downs, R.T., Bish, D.L., Ming, D.W., Edgett, K.S., Rubin, D., Goetz, W., and others and MSL Science

Team (2013) Curiosity at Gale Crater, Mars: Characterization and analysis of the Rocknest Sand Shadow. Science, 341, 1239505.
Bristow, T.F., Bish, D.L., Vaniman, D.T., Morris, R.V., Blake, D.F., Grotzinger, J.P., Rampe, E.B., Crisp, J.A., Achilles, C.N., Ming, D.W., and others. (2015) The origin and implications of clay minerals from Yellowknife Bay, Gale crater, Mars. American Mineralogist, 100, 824–836.
Cameron, M., and Papike, J.J. (1981) Structural and chemical variations in pyroxenes. American Mineralogist, 66, 1–50.
Dal Negro, A., De Pieri, R., Quareni, S., and Taylor, W.H. (1978) The crystal structures of nine K feldspars from Adamello Massiff (Northern Italy). Acta Crystallographica, B34, 2699–2707.
Fisher, G.W., and Medaris, L.G. (1969) Cell dimensions and X-ray determinative curve for synthetic Mg-Fe olivines. American Mineralogist, 54, 741–753.
Gay, D.M. (1990) Usage summary for selected optimization routines. Computing Science Technical Report 153, AT&T Bell Laboratories, Murray Hill.
Golden, D.C., Ming, D.W., Morris, R.V., and Graff, T.G. (2008) Hydrothermal synthesis of hematite spherules and jarosite—Implications for diagenesis and hematite spherule formation in sulphate outcrops at Meridiani Planum, Mars. American Mineralogist, 93, 1201–1214.
Hewins, R.H., Zanda, B., Humayun, M., Nemchin, A., Lorand, J.P., Pont, S., Deldicque, D., Bellucci, J.J., Beck, P., Leroux, H., and Marinova, M. (2017) Regolith breccia Northwest Africa 7533: Mineralogy and petrology with implications for early Mars. Meteoritics & Planetary Science, 52(1), 89–124.
Jahanbagloo, I.C. (1969) X-ray diffraction study of olivine solid solution series. American Mineralogist, 54, 246–250.
Klingelhöfer, G., Morris, R.V, Bernhardt, B., Schröder, C., Rodionov, D.S., de Souza, P.A., Yen, A., Gellert, R., Evlanov, E.N., Zubkov, B., and others. (2004) Jarosite and hematite at Meridiani Planum from Opportunity's Mössbauer spectrometer. Science, 306, 1740–1745.
Kroll, H. (1983) Lattice parameters and determinative methods for plagioclase and ternary feldspars. Reviews in Mineralogy, 2, 101–119.
Kroll, H., and Ribbe, P.J. (1983) Lattice parameters, composition and Al,Si order in alkali feldspars. Reviews in Mineralogy, 2, 57–100.
Kuehner, S.M., and Joswiak, D.J. (1996) Naturally occurring ferric iron sanidine from the Leucite Hills lamproite. American Mineralogist, 81, 229–237.
Lafuente, B., Downs, R.T., Yang, H., and Stone, N. (2015) The power of databases: the RRUFF project. Highlights in Mineralogical Crystallography, 1–30 p.
Lebedeva, Y.S., Pushcharovsky, D.Y., Pasero, M., Merlino, S., Kashaev, A.A., Taroev, V.K., Goettlicher, J., Kroll, H., Pentinghaus, H., Suvorova, L.F., and Wulf-Bernodat, H. (2003) Synthesis and crystal structure of low ferrialuminosilicate sanidine. Crystallography Reports, 48(6), 919–924.
Linthout, K., and Lustenhouwer, W.J. (1993) Ferrian high sanidine in a lamproite from Cancarix, Spain. Mineralogical Magazine, 57(2), 289–299.
Louisnathan, S.J., and Smith, J.V. (1968) Cell dimensions of olivine. Mineralogical Magazine, 36, 1123–1134.
Matsui, T., and Kimata, M. (1997) Crystal chemistry of synthetic Mn-bearing anorthite; incorporation of $MnAl_2Si_2O_8$ end-member into feldspar. European Journal of Mineralogy, 9(2), 333–344.
Matsui, Y., and Syono, Y. (1968) Unit cell dimensions of some synthetic olivine group solid solutions. Geochemical Journal, 2, 51–59.
Mills, S.J., Nestola, F., Kahlenberg, V., Christy, A.G., Hejny, C., and Redhammer, G.J. (2013) Looking for jarosite on Mars: The low-temperature crystal structure of jarosite. American Mineralogist, 98, 1966–1971.
Morris, R.V., Klingelhoefer, G., Schröder, C., Rodionov, D.S., Yen, A., Ming, D.W., De Souza, P.A., Fleischer, I., Wdowiak, T., Gellert, R., and Bernhardt, B. (2006a) Mössbauer mineralogy of rock, soil, and dust at Gusev crater, Mars: Spirit's journey through weakly altered olivine basalt on the plains and pervasively altered basalt in the Columbia Hills. Journal of Geophysical Research: Planets, 111, E02S13.
Morris, R.V., Klingelhöfer, G., Schröder, C., Rodionov, D.S., Yen, A., Ming, D.W., de Souza, P.A., Wdowiak, T., Fleischer, I., Gellert, R., and others (2006b) Mössbauer mineralogy of rock, soil, and dust at Meridiani Planum, Mars: Opportunity's journey across sulfate-rich outcrop, basaltic sand and dust, and hematite lag deposits. Journal of Geophysical Research: Planets, 111, E12S15.
Morris, R.V., Klingelhöfer, G., Schröder, C., Fleischer, I., Ming, D.W., Yen, A.S., Gellert, R., Arvidson, R.E., Rodionov, D.S., Crumpler, L.S., and others. (2008) Iron mineralogy and aqueous alteration from Husband Hill through Home Plate at Gusev Crater, Mars: results from the Mössbauer instrument on the Spirit Mars Exploration Rover. Journal of Geophysical Research: Planets, 113, E12S42.
Morris, R.V., Vaniman, D.T., Blake, D.F., Gellert, R., Chipera, S.J., Rampe, E.B., Ming, D.W., Morrison, S.M., Downs, R.T., Treiman, A.H., and others. (2016) Silicic volcanism on Mars evidenced by tridymite in high-SiO_2 sedimentary rock at Gale crater. Proceedings of the National Academy of Sciences, 113, 7071–7076.
Morrison, S.M., Downs, R.T., Blake, D.F., Vaniman, D.T., Ming, D.W., Rampe, E.B., Bristow, T.F., Achilles, C.N., Chipera, S.J., Yen, A.S., and others. (2018) Crystal chemistry of martian minerals from Bradbury Landing through Naukluft Plateau, Gale crater, Mars. American Mineralogist, 103, 857–871.
Nolan, J. (1969) Physical properties of synthetic and natural pyroxenes in the system diopsite-hedenbergite-acmite. Mineralogical Magazine, 37, 216–229.
Nyquist, L.E., Shih, C.Y., McCubbin, F.M., Santos, A.R., Shearer, C.K., Peng, Z.X., Burger, P.V., and Agee, C.B. (2016) Rb-Sr and Sm-Nd isotopic and REE studies of igneous components in the bulk matrix domain of Martian breccia Northwest Africa 7034. Meteoritics & Planetary Science, 51(3), 483–498.
Papike, J.J. (1980) Pyroxene mineralogy of the Moon and meteorites. Reviews in Mineralogy, 7, 495–525.
Papike J.J., Ryder G., and Shearer C.K. (1998) Lunar samples. Reviews in Mineralogy, 36, 5.1–5.234.
Papike, J.J., Karner, J.M., Shearer, C.K., and Burger, P.V. (2009) Silicate mineralogy of martian meteorites. Geochimica et Cosmochimica Acta, 73, 7443–7485.
Rampe, E.B. Ming, D.W., Blake, D.F., Vaniman, D.T., Chipera, S.J., Bristow, T.F., Morris, R.V., Yen, A.S., Morrison, S.M., Grotzinger, J.P., and others. (2017) Mineralogical trends in mudstones from the Murray formation, Gale crater, Mars. Earth and Planetary Science Letters, 471, 172–185.
Robinson, P. (1980) The composition space of terrestrial pyroxenes; internal and external limits. Reviews in Mineralogy, 7, 419–494.
Rutstein, M.S., and Yund, R.A. (1969) Unit-cell parameters of synthetic diopside-hedenbergite solid solutions. American Mineralogist, 54, 238–245.
Santos, A.R., Agee, C.B., McCubbin, F.M., Shearer, C.K., Burger, P.V., Tartese, R., and Anand, M. (2015) Petrology of igneous clasts in Northwest Africa 7034: Implications for the petrologic diversity of the Martian crust. Geochimica et Cosmochimica Acta, 157, 56–85.
Schwab, R.B., and Kustner, D. (1977) Präzisionsgitterkonstantenbestimmung zur festlegung röntgenographischer Bestimmungskurven für synthetische Olivin der Mischkristallreihe Forsterit-Fayalit. Neues Jahrbuch für Mineralogie, Monatshefte, 205–215.
Smith, J.V. (1974) Feldspar Minerals, Springer-Verlag, Berlin.
Swayze, G.A., Desborough, G.A., Smith, K.S., Lowers, H.A., Hammarstrom, J.M., Diehl, S.F., Leinz, R.W., and Driscoll, R.H. (2008) Understanding jarosite—From mine waste to Mars. U.S. Geological Survey Circular 1328, p. 8–13.
Treiman, A.H., Morris, R.V., Agresti, D.G., Graff, T.G., Achilles, C.N., Rampe, E.B., Bristow, T.F., Ming, D.W., Blake, D.F., Bish, D.L., and others. (2014) Ferrian saponite from the Santa Monica Mountains (California, U.S.A., Earth): Characterization as an analog for clay minerals on Mars with application to Yellowknife Bay in Gale crater. American Mineralogist, 99, 2234–2250.
Treiman, A.H., Bish, D.L., Vaniman, D.T., Chipera, S.J., Blake, D.F., Ming, D.W., Morris, R.V., Bristow, T.F., Morrison, S.M., Baker, M.B., and others. (2016) Mineralogy, provenance, and diagenesis of a potassic basaltic sandstone on Mars: CheMin X-ray diffraction of the Windjana sample (Kimberley area, Gale Crater). Journal of Geophysical Research: Planets, 121, 75–106.
Turnock, A.C., Lindsley, D.H., and Grover, J.E. (1973) Synthesis and unit cell parameters of Ca-Mg-Fe pyroxenes. American Mineralogist, 58, 50–59.
Vaniman, D.T., Bish, D.L., Ming, D.W., Bristow, T.F., Morris, R.V., Blake, D.F., Chipera, S.J., Morrison, S.M., Treiman, A.H., Rampe, E.B., and others and MSL Science Team. (2014) Mineralogy of a Mudstone at Yellowknife Bay, Gale Crater, Mars. Science, 343, 1–9.
Wittmann, A., Korotev, R.L., Jolliff, B.L., Irving, A.J., Moser, D.E., Barker, I., and Rumble, D. (2015) Petrography and composition of Martian regolith breccia meteorite Northwest Africa 7475. Meteoritics & Planetary Science, 50(2), 326–352.
Yen, A.S., Ming, D.W., Vaniman, D.T., Gellert, R., Blake, D.F., Morris, R.V., Morrison, S.M., Downs, R.T., Bristow, T.F., Clark, B.C., and others and the MSL Science Team. (2017) Multiple episodes of aqueous alteration along fractures in mudstone and sandstone in Gale crater, Mars. Earth and Planetary Science Letters, 471, 186–198.
Yoder, H.S. Jr., and Sahama, T.G. (1957) Olivine X-ray determinative curve. American Mineralogist, 42, 475–491.
Zolotov, M.Y., and Shock, E.L. (2005) Formation of jarosite-bearing deposits through aqueous oxidation of pyrite at Meridiani Planum, Mars. Geophysical Research Letters, 32, L21203.

Manuscript received February 27, 2017
Manuscript accepted November 19, 2017
Manuscript handled by Bradley Jolliff

Endnote:

[1]Deposit item AM-18-66123, Appendix, Supplemental Tables, and Figures. Deposit items are free to all readers and found on the MSA web site, via the specific issue's Table of Contents (go to http://www.minsocam.org/MSA/AmMin/TOC/2018/Jun2018_data/Jun2018_data.html).